The Astrophysical Journal Supplement Series, 269:26 (10pp), 2023 November https://doi.org/10.3847/1538-4365/acfd99

Infrared Spectral Fingerprint of Neutral and Charged Endo- and Exohedral Metallofullerenes

R. Barzaga[1,2], D. A. García-Hernández[1,2], S. Díaz-Tendero[3,4,5], SeyedAbdolreza Sadjadi[6], A. Manchado[1,2,7], M. Alcami[3,4,8], M. A. Gómez-Muñoz[1,2], and T. Huertas-Roldán[1,2]
[1] Instituto de Astrofísica de Canarias, C/ Vía Láctea s/n, E-38205 La Laguna, Spain; rbarzaga@iac.es
[2] Departamento de Astrofísica, Universidad de La Laguna (ULL), E-38206 La Laguna, Spain
[3] Departmento de Química, Módulo 13, Universidad Autónoma de Madrid, E-28049 Madrid, Spain
[4] Institute for Advanced Research in Chemical Science (IAdChem), Universidad Autónoma de Madrid, E-28049 Madrid, Spain
[5] Condensed Matter Physics Center (IFIMAC), Universidad Autónoma de Madrid, E-28049 Madrid, Spain
[6] Laboratory for Space Research, Faculty of Science, The University of Hong Kong, Hong Kong (SAR), People's Republic of China
[7] Consejo Superior de Investigaciones Científicas (CSIC), Spain
[8] Instituto Madrileño de Estudios Avanzados en Nanociencia (IMDEA-Nano), Campus de Cantoblanco, Madrid E-28049, Spain
Received 2023 June 23; revised 2023 August 28; accepted 2023 September 19; published 2023 November 6

Abstract

Small metal-containing molecules have been detected and recognized as one of the hybrid species that are efficiently formed in space, especially in the circumstellar envelopes of evolved stars. It has also been predicted that more complex hybrid species such as those formed by metals and fullerenes (metallofullerenes) could be present in these circumstellar environments. Recently, quantum-chemical simulations of metallofullerenes have shown that they are potential emitters contributing to the observed mid-IR spectra in the fullerene-rich circumstellar environments of different types of evolved stars. Here we present the individual simulated mid-IR (∼5–50 μm) spectra of 28 metallofullerene species. Both neutral and charged endo- and exohedral metallofullerenes for seven different metals (Li, Na, K, Ca, Mg, Ti, and Fe) have been considered. The changes induced by the metal–C_{60} interaction in the intensity and position of the spectral features are highlighted using charge-density difference maps and electron-density partitioning. Our calculations identify the fundamental IR spectral regions in which, depending on the metal binding nature, there should be a major spectral contribution from each of the metallofullerenes. The IR spectra of the metallofullerenes are made publicly available to the astronomical community, especially users of the James Webb Space Telescope, for comparisons that could eventually lead to the detection of these species in space.

Unified Astronomy Thesaurus concepts: Quantum-chemical calculations (2232); Astrochemistry (75); Infrared spectroscopy (2285)

1. Introduction

More than 240 molecules (formed by up to 19 different chemical elements) have been detected in space so far (see, e.g., McGuire 2022, for a recent review). Different individual molecular species are detected in a variety of cosmic environments, from interstellar/circumstellar media to protoplanetary disks and exoplanet atmospheres and distant galaxies, among others (McGuire 2022). The great majority (∼70%) of them are organic (carbon-containing) species, which are mainly detected in the insterstellar and circumstellar medium. Interestingly, metal-containing organic molecules (i.e., with metals such as Mg, Na, Al, K, Fe, and Ca) have only been detected in the circumstellar envelopes of evolved stars, especially toward the nearby and bright (prototype) C-rich evolved star IRC +10216 (e.g., Cernicharo & Guelin 1987, but see also Cernicharo et al. 2023 for the most recent detections of metal-containing organic species toward IRC+10216).

The strong mass loss experienced by low- and intermediate-mass (∼1–8 $M_{\odot}$) evolved stars during the asymptotic giant branch (AGB) stage causes the enrichment of the surrounding circumstellar and interstellar medium with the heavier elements (metals and even heavier s-process elements) that were previously produced inside the star by stellar nucleosynthesis (Karakas & Lattanzio 2014). The subsequent post-AGB evolution toward the formation of planetary nebulae (PNe), however, occurs with almost no mass loss or additional stellar nucleosynthesis (e.g., Jones 2017; Kwitter & Henry 2022, and references therein). A metal enrichment of the circumstellar environment not only occurs for PNe precursors, but also in other types of astrophysical objects, e.g., the chemically peculiar R Coronae Borealis (RCB) stars (e.g., Montiel et al. 2018; Schwab 2019; Pandey et al. 2021). In these environments, chemical processes take place to form both simple and more complex organic species such as fullerenes (Cami et al. 2010; García-Hernández et al. 2010, 2011), but the formation of other organic species containing alkaline to transition metals is also possible.

Thus, the coexistence of organic species and metals in the circumstellar environment of evolved stars can give rise to more complex metal-organic compounds; i.e., hybrid species containing both. The detection of metal-containing organic molecules such as MgNC and NaCN in the circumstellar envelopes around AGB stars and PNe are undeniable examples (e.g., Highberger et al. 2001; Ziurys 2006; McGuire 2022). Previous experimental studies supported by quantum-chemistry calculations have also demonstrated that fullerenes can react with metals forming endo- and exohedral metallofullerenes (e.g., Dunk et al. 2013). This has a significant relevance

because fullerenes, mainly C_{60}, which is characterized by its four strongest mid-IR features at ∼7.0, 8.5, 17.4, and 18.9 μm, have been detected in young PNe and RCB stars (see Cami et al. 2010; García-Hernández et al. 2010, 2011). PNe and RCB stars also have abundant metals residing in their circumstellar envelopes, and it is thus reasonable to assume that metals would react with fullerenes to produce metallofullerenes.

In order to explore the possible existence of metallofullerenes in fullerene-rich circumstellar envelopes, we have previously performed quantum-chemistry calculations of the IR vibrational spectra of charged and neutral endo- and exohedral metallofullerenes (Barzaga et al. 2023). According to the IR spectra simulation (i.e., the total and total-weighted metallofullerene spectra; see Barzaga et al. 2023), the presence of metallofullerenes could explain the large range of C_{60} 17.4 μm/18.9 μm band ratios observed in PNe and RCB stars. Therefore, metallofullerenes can be considered as potential emitters that contribute to the observed IR spectra in the fullerene-rich circumstellar envelopes of these types of objects.

In this work, we focus on the individual simulated mid-IR (∼5−50 μm) spectra of the 28 metallofullerene species, i.e., neutral and charged endo- and exohedral metallofullerenes for the seven different metals Li, Na, K, Ca, Mg, Ti, and Fe. These metals were selected because they are most abundant and/or are well known to exist in the interstellar medium. According to nucleosynthesis models and published abundances, they are also among the most abundant metals in low-mass evolved stars such as PNe and RCB stars (see, e.g., Jeffery et al. 2011; Karakas & Lattanzio 2014), and thus, they are more likely to react with fullerenes (see also Barzaga et al. 2023, for more details). We analyze the charge redistribution in the C_{60} carbon cage induced by the metal along with the carbon-metal bond strength and bonding sites, in order to rationalize the changes in the IR intensity and position of the spectral features. To this end, charge-density difference mapping and electron-density partitioning have been performed. Both methods allowed us to identify the metal-C_{60} interaction effect on the intensity/position of the IR features for the several metallofullerenes. We aim to provide the IR spectra of the metallofullerenes to the astrophysical community, in particular, to users of the James Webb Space Telescope, for a future spectral match that could eventually lead to the first detection of these complex metal-organic species in space.

2. Computational Details

Calculations of the neutral/charged endo- (inside C_{60}) and exohedral (outside C_{60}) metallofullerenes have been performed in the framework of density functional theory (DFT) at the B3LYP/6-31G(d) level (Ditchfield et al. 1971; Becke 1993), with the Gaussian 16 code (Frisch et al. 2016), following the settings reported in our previous work (Barzaga et al. 2023).[9] The mid-IR spectra were obtained under the harmonic oscillator approximation, and subsequently, wavelengths were adjusted using double scaling factors to account for anharmonicity, vibrorotational coupling, and so on. The maximum error obtained under this approach in the calculated wavelength was <2%; previous work has demonstrated the accuracy of this procedure (Robledo et al. 2014; Zapata Trujillo & McKemmish 2022). To facilitate comparison of the several simulated mid-IR spectra, the peak profile has been modeled by a Lorentzian function with an FWHM = 0.02 μm, which reproduces the average resolution ($R \sim 1700$) of the Mid-IR Instrument (∼5−30 μm) on board the James Webb Space Telescope (JWST; but see also below). A Lorentzian function is a more adequate profile of the peak in order to relate molecular structure with the IR spectral signature because it describes a peak width invariant around a central wavelength (as expected in gas-phase species) and it reflects the natural width (natural damping and pressure broadening; see, e.g., Pradhan & Nahar 2011). Moreover, the former property of the Lorentzian function has been extensively used to reproduce the observed spectral profiles of some unidentified IR bands and diffuse interstellar bands (e.g., Pech et al. 2002; Snow et al. 2002). All individual simulated spectra are available on Zenodo at doi:10.5281/zenodo.8215397. In any case, the intensity and wavelength of the IR lines are also provided in this paper to allow the astrophysical community the convolution with any peak function; e.g., to obtain simulated spectra at different resolutions and spectral profiles.

Quantum theory of atoms in molecules, employing the AimAll software, has been applied to characterize the bonding type and strength by using the topological analysis of the electron-density distribution (Bader 1990; Keith 2019). The former analysis permits the extraction of the kinetic (G), potential (V), and total ($H = G + V$) energy densities, with V and G always negative and positive, respectively (Cremer & Kraka 1984; Bader 1990). By employing the $|V|/G$ ratio, it is possible to determine the bonding type according to the formula that $|V|/G < 1$ indicates a pure ionic bond, while $|V|/G > 2$ corresponds to a pure covalent bond and $1 > |V|/G > 2$ indicates a bond in between (Zabardasti et al. 2017; Barzaga et al. 2021). The bond strength is identified by the amount of electron density (ρ) in the internuclear region of a bond. It is important to note that the topological analysis of the electron density allows an automatic identification of the bonding nature between atoms. Thus, it is possible to determine direct metal-fullerene connections. Finally, charge-density difference (CDD) maps were presented in order to illustrate the charge reordering induced by the metal in the carbon cage. The CDD mapping describes the regions within the electron density that experience an increase (accumulation) or decrease (depletion) in electrons upon metal-fullerene interaction.

3. Results

First, we consider the analysis of the individual mid-IR spectra for the different metallofullerenes, tracking the particular spectral features that define the metal–C_{60} cage interaction for each case. To facilitate comparison, Figures 1–4 (representing all individual neutral and charged endo- and exohedral metallofullerenes spectra) also include the total (summed) spectrum for each metallofullerene species, constructed similarly to our previous work (Barzaga et al. 2023). The IR intensities of the individual simulated spectra are scaled to the same total value. In this way, we guarantee that all spectra are at the same intensity level, even though they are vertically offset for better visualization. In addition, in order to preserve the intensity for each metallofullerene species, exo- or endofullerene, the spectra were also multiplied by a scaling factor. In Figures 1–4, we display the spectral range from 5 to 25 μm, while the full range (5–50 μm) IR spectra can be found in Zenodo:

[9] In particular, the metals were placed in different binding sites of the C_{60} cage before geometry optimization: in the hexagon–hexagon bond region, in the center of a hexagon, directly above a carbon, in the pentagon–hexagon bond, in the center of a pentagon, and in the center of the cage. After geometry optimization, the most stable structure was selected for each type of metallofullerene (see Table 1). In addition, for all the calculations, spin multiplicity (2S + 1) has been considered up to a maximum of S = 5/2.

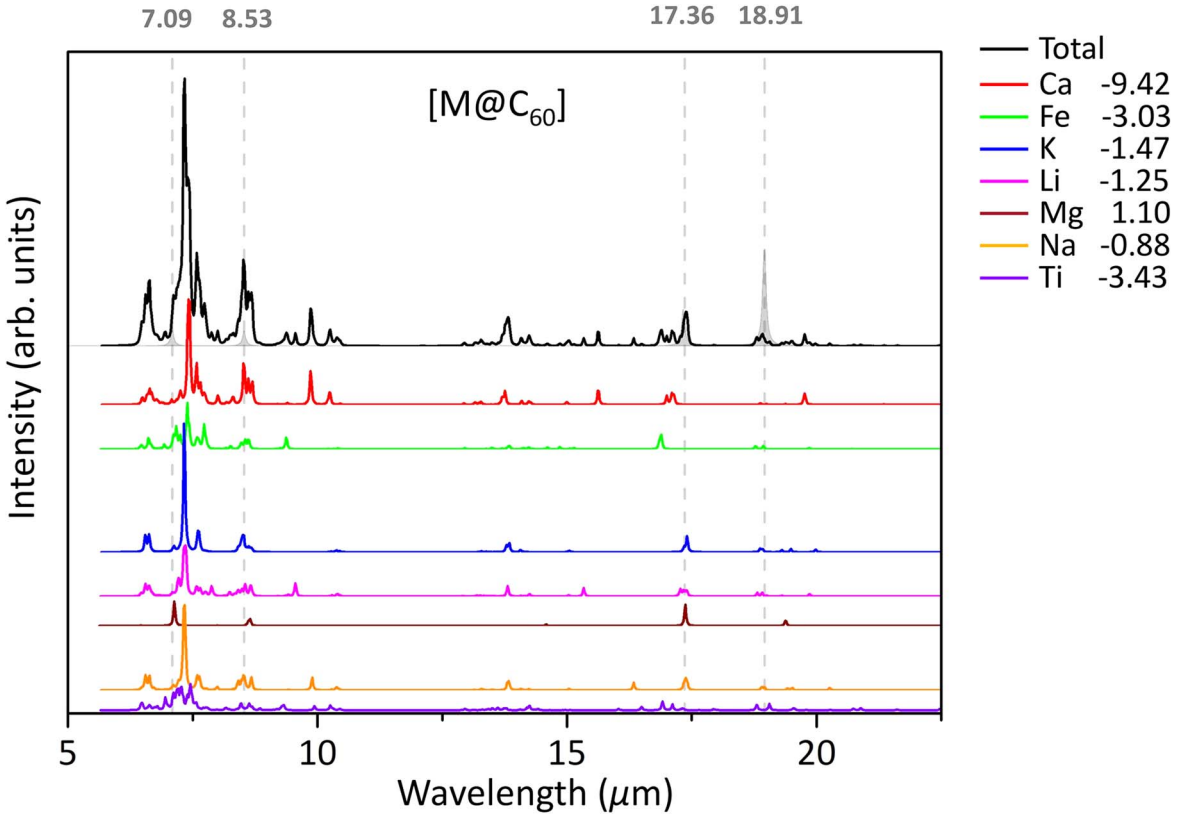

Figure 1. Total (black) and individual spectra of neutral metalloendofullerenes [M@C_{60}] in the 5–25 μm range for seven different metals (Li, Na, K, Ca, Mg, Ti, and Fe). In the case of Ti ([Ti@C_{60}]), an intensity offset has been applied to facilitate the visualization. The legend plot shows the color code we used to represent the individual neutral metalloendofullerene spectra. The dashed vertical gray lines and shaded peaks indicate the four strongest IR features of pristine C_{60} at the DFT B3LYP/6-31G level of theory. In addition, binding energies (eV) concerning the metal-C_{60} bond are also added for each metal. The full range (5–50 μm) of the mid-IR spectra can be found in the corresponding appended data.

doi:10.5281/zenodo.8215397. The four strongest features of pristine C_{60} are also overplotted in Figures 1–4 for comparison purposes and to represent the real difference in their IR intensity against the metallofullerene species. In addition, the binding energies (in eV) are also provided in the figures to show the strength of the metal–C_{60} bond; negative values reflect a stronger binding. Subsequently, after the spectrum analysis, a thorough analysis of the nature of the metal–C_{60} bond is carried out in order to characterize it as ionic, covalent, or in between. The former is also used to relate the spectral fingerprint of metallofullerenes to its molecular structure.

3.1. Metalloendofullerenes

The individual IR spectra of the neutral endofullerene [M@C_{60}] are shown in Figure 1, highlighting the different metal species with different colors. There are two specific regions in these spectra that contain the four pristine C_{60} IR features (see, e.g., Kern et al. 2013; Barzaga et al. 2023): (i) the 5–10 μm C–C stretching vibrations, and (ii) the 15–20 μm C_{60} cage vibrations. The C–C stretching region shows a common trend for Li, Na, and K (alkaline metals) neutral endofullerenes. Multiple features can be distinguished in this region, with an intense peak at 7.34 μm accompanied by a prominent shoulder like in the case of Li. These three alkaline endofullerenes exhibit different peaks in the 15–17 μm spectral region, although they display a unique feature centered at ~13.82 μm. The difference between Li, Na, and K is noticeable in terms of the feature intensity in the 5–10 μm region, especially around 7.3 μm, with K showing the most intense feature but poorer spectra (see Figure 1 and the appended data). The next sorted group of neutral endofullerenes are Fe and Ti, which exhibit IR features with a similar positioning in the C–C stretching region of the spectra, but which are not comparable in terms of intensity. The main characteristic of the Fe and Ti neutral endofullerenes is the low feature intensity throughout the full spectral region. On the other hand, the Ca neutral endofullerene shows the richest IR spectrum of all neutral metalloendofullerenes; its IR spectrum resembles that of others species in some regions, but it is not possible to find a very similar spectrum among the rest of the endofullerene spectra. Interestingly, the IR spectrum of the Mg neutral endofullerene remains almost identical to that of pristine C_{60}, without any indication of additional emission features in the C–C stretching and C_{60} cage vibration regions. In general, all neutral endofullerenes show a significant loss of feature intensity around 18.5–19 μm, which is the region with the highest-intensity features for pristine C_{60}. Finally, the contribution to the total (summed) neutral metallonendofullerene spectrum (black line in Figure 1) is dominated by Ca > K > Li in that order, with Mg contributing least.

In the case of charged metalloendofullerenes $[M@C_{60}]^+$, the contribution trend in the mid-IR spectra is hindered by a decrease in the global feature intensity with respect to the neutral ones (see the scaling factor used in Figure 2). The richer IR spectra observed here correspond to the charged endofullerenes with Ca, Li, Ti, Fe, and Mg. From this group, the Ca-charged endofullerene exhibits the highest feature intensity and

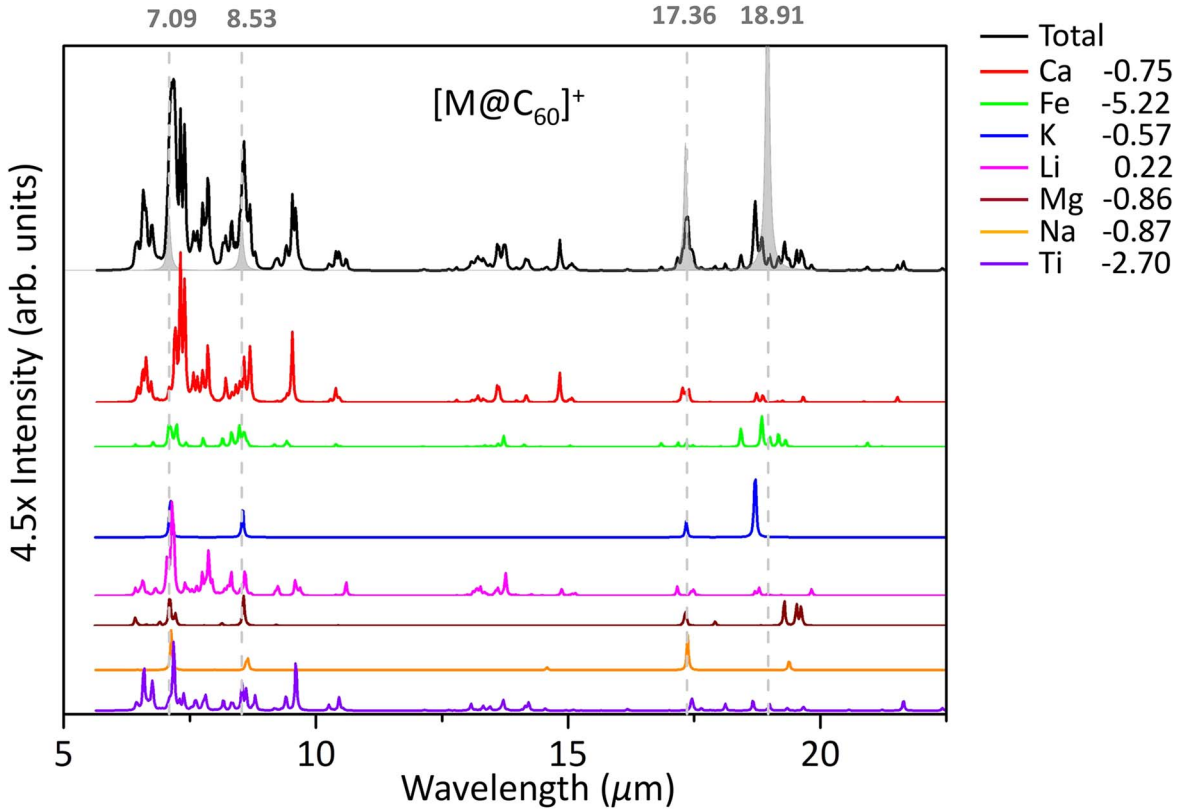

Figure 2. Total (black) and individual spectra of charged metalloendofullerenes $[M@C_{60}]^+$ in the 5–25 μm range for seven different metals (Li, Na, K, Ca, Mg, Ti, and Fe). As in Figure 1, the legend plot shows the color code we used to represent the individual charged metalloendofullerene spectra, and the binding energies (eV), while the pristine C_{60} features are marked with vertical gray lines and shaded peaks. Note that this time, the intensities are multiplied by a factor of 4.5 in order to match Figure 1. Again, the full range (5–50 μm) of the mid-IR spectra can be found in the corresponding appended data.

remains the main contributor to the total (summed) charged metallofullerene spectrum (black line in Figure 2). Again, in the 5–10 μm C–C stretching region, the spectral modifications are more noticeable, indicating the effect of the metal binding to the carbon cage. In contrast, the Na- and K-charged endofullerene spectra, when compared with pristine C_{60}, display almost unperturbed spectra, which might be an indication of a weaker metal-carbon cage binding in principle. However, the binding energy values displayed in Figure 2 do not reflect this possible trend because Li is the weakest bonded metal. Thus, another intrinsic effect should be playing a role here, as we discuss further below. In Figure 2 we can also observe the lack of a trend in the spectrum landscape of the charged metalloendofullerenes, which indicates different effects of the metal–C_{60} interactions. For example, the Na- and K-charged endofullerene IR spectra are the most similar, according to the feature position; for the remaining charged endofullerenes, however, there is a diversity of IR bands that are specific to each species. These observations indicate a significant change in the nature and strength of the metal–C_{60} interaction, depending on the metal, when the molecular system is charged. Consequently, the total (summed) spectrum (black line Figure 2) becomes spectrally broader, weaker, and richer because fewer species contribute to the same spectral region.

3.2. Metalloexofullerenes

The metalloexofullerenes have the advantage that the metal binds externally to the carbon cage, allowing us to accommodate it and establishing a more efficient and stronger interaction than in their endohedral analogs. The C–C stretching region (5–10 μm) in each metalloexofullerene spectrum reflects this behavior with multiple IR bands of medium or high intensity. In particular, the IR spectra of neutral exofullerenes [M-C_{60}] (see Figure 3) with K, Li, Na, and seemingly Ca, are the most similar ones. Their spectra are characterized by a double peak at 7.26 μm of different intensity, which is surrounded by medium-intensity and relatively broad satellite bands. Another unique feature of these species is observed at 9.37–9.43 μm as an isolated band, while a single band at 17.42 μm (coincident with pristine C_{60}) always appears in the C_{60} cage vibration region (15–20 μm). Both features are also present for the Mg neutral exofullerene, but the rest of the spectrum is very different. Finally, the Fe and Ti neutral exofullerene IR spectra form a separate group with an almost full coincidence (both in intensity and position) in their spectral features and a distinctive broad band at 19.05 μm. It is worth noting that all neutral exofullerene IR spectra exhibit a higher intensity than their endohedral counterparts (see the scaling factors used in Figures 1 and 3), which reinforces the importance of the charge rearrangement processes. The metal is externally bonded to the carbon cage, creating a system in which charge transfer takes place C_{60}^{-} M^{+} (see, e.g., Barzaga et al. 2023), and thus resulting in a strong modification of the dipole moment, and consequently, of the IR intensity.

As expected, charged metalloexofullerenes display weaker IR spectra (see Figure 4), but with spectral features lying very close to those of the pristine C_{60}, as calculated by us at the same theoretical level (i.e., at 7.09, 8.53, 17.36, and 18.91 μm). In this case, the charge redistribution induced by the cation creates a system like C_{60}^{0} M^{+} (see, e.g., Barzaga et al. 2023),

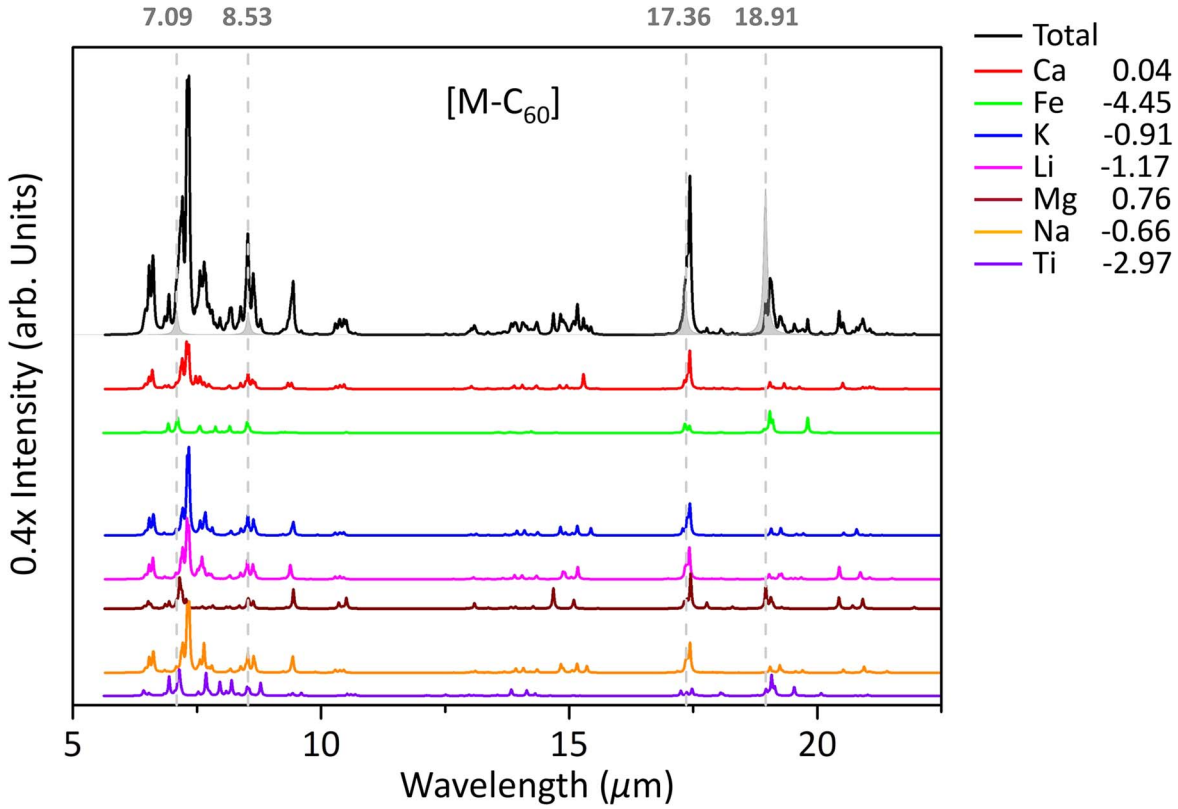

Figure 3. Total (black) and individual spectra of neutral metalloexofullerenes [M-C_{60}] in the 5–25 μm range for seven different metals (Li, Na, K, Ca, Mg, Ti, and Fe). As in Figure 1, the legend plot shows the color code we used to represent the individual neutral metalloexofullerene spectra, and the binding energies (eV), while the pristine C_{60} features are marked with vertical gray lines and shaded peaks. Note that this time, the intensities are multiplied by a factor of 0.4 (i.e., the feature intensities are higher than in Figure 1) in order to match Figure 1. Again, the full range (5–50 μm) of the mid-IR spectra can be found in the corresponding appended data.

which likely reduces the changes in the dipole moment and thus produces a lower IR feature intensity. In general, all charged metalloexofullerenes show strong similarities in their spectra, with the exception of the Fe and Ti ones. The IR-simulated spectra are characterized by a single band at 6.41 μm and a doublet centered at ~7.13 μm, which can be symmetric for K, Na, and Li and asymmetric for Ca and Mg. This doublet seems to be absent for the Fe- and Ti-charged exofullerene species, which otherwise display an additional band around ~8.53 μm (i.e., coincident with pristine C_{60}). It is to be noted here that only the 6.41 μm band is free from any contribution from the pristine C_{60} features. At longer wavelengths (i.e., 15–20 μm), the charged exofullerenes display a very similar spectral behavior: a band at 17.33 μm and a doublet centered at 18.98 μm, both contributing to the pristine C_{60} IR features. Curiously, the Fe- and Ti-charged exofullerenes are exceptions in this region, showing broader features and richer spectra, respectively.

3.3. Bonding Nature

The basics of IR spectroscopy are determined by two equations: one equation is obtained from the harmonic oscillator approximation $\left(\bar{\nu} = \frac{1}{2\pi c}\sqrt{\frac{k}{u}}\right)$[10], which describes the position (wavelength) of the spectral features. Here the key factor is the force constant k, related to the modification of the bond strength. The second expression affecting IR spectroscopy denotes the dependence of the IR intensity on the dipole moment change ($\partial\mu$), as caused by the vibration displacement (∂x) $I \propto \frac{\partial \mu}{\partial x}$. A modification of the dipole moment can be induced by a strong reordering of the electron-density charge, but also by larger vibrational displacements, which hence produce a large dipole moment, and thus a higher intensity. Therefore, in order to make a more exhaustive analysis of the simulated metallofullerene spectra and to infer the origin of the most characteristic features, we have studied the strength and type of the metal-C_{60} bonding, and we mapped the charge reordering in the cage induced by the metal.

Figures 5 and 6 represent the charge reordering induced in the carbon cage by the presence of the metal for the endo and exo cases, respectively. The regions in which a greater accumulation of electrons appears due to the metal presence are depicted in light blue, while the light red area encloses regions with fewer electrons. From a first inspection, a higher IR intensity of the exofullerene spectra in comparison to their endofullerene counterparts is clear. In contrast to the endofullerenes, the exofullerenes have the metal outside the cage, which creates a larger dipole moment change due to the vibration, which in turn increases the IR intensity. In addition, the charge reordering in the exofullerene creates a significant dipole moment change in comparison to their charged analogs, which is caused by a depletion and accumulation of electrons at the border of the carbon cage. This behavior is marked for the

[10] This expression is already modified to determine the wavenumber ($\bar{\nu}$) of the vibration by adding the speed-of-light constant (c). The corresponding conversion factor should be applied in order to obtain wavelength units. In addition, u here represents the reduced mass, and this notation has been used to avoid confusion with the dipole moment (μ).

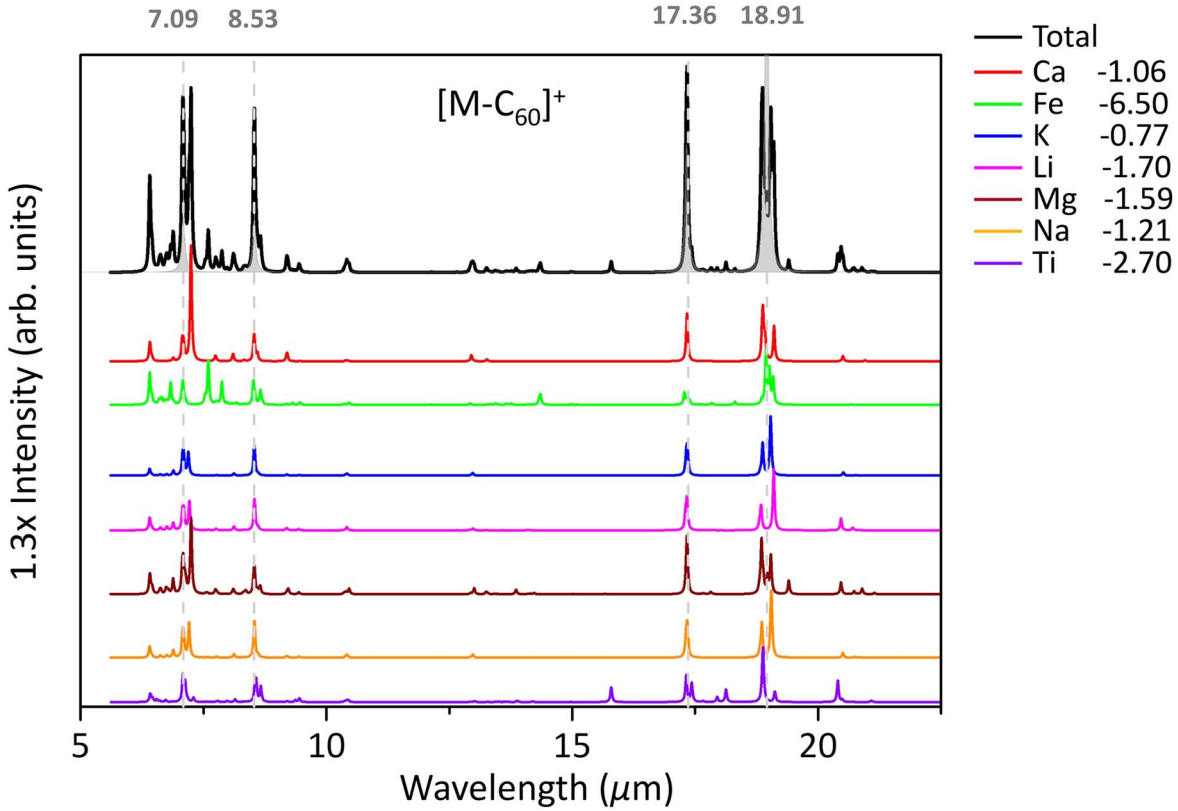

Figure 4. Total (black) and individual spectra of charged metalloexofullerenes $[M\text{-}C_{60}]^+$ in the 5–25 μm range for seven different metals (Li, Na, K, Ca, Mg, Ti, and Fe). As in Figure 1, the legend plot shows the color code we used to represent the individual charged metalloexofullerene spectra, and the binding energies (eV), while the pristine C_{60} features are marked with vertical gray lines and shaded peaks. Note that this time, the intensities are multiplied by a factor of 1.3 in order to match Figure 1. Again, the full range (5–50 μm) of the mid-IR spectra can be found in the corresponding appended data.

neutral exofullerenes with K, Na, and Li; this explains the high IR intensity observed in Figure 3. The neutrality in the endofullerenes shows the same behavior, but at a lower level. The former is caused by a smaller dipole moment as a consequence of the charge reordering implying the whole carbon cage. Thus, the dipole moment is of lower magnitude on average. It is worth noting that the metal in neutral endofullerenes has smaller vibrational displacements that also contribute to reducing the IR intensity. This intensity reduction is stronger when a larger charge reordering takes place, and it diminishes the dipole moment, as in the case of charged endofullerenes (see the intensity scales in Figures 1 and 2). Another aspect reinforcing our analysis is the bonding type of the different metallofullerenes, as described by the $|V|/G$ ratio (see Section 2) and represented in Figures 5 and 6. Predominantly, the metallofullerenes exhibit ionic bondings ($|V|/G < 1$), indicating that the electrostatic interactions dominate, and enhancing large dipole moment changes. When the ionic character of the bonds is weakened (Fe, Mg, Ti, $|V|/G \geqslant 1$), the IR intensity drastically drops in comparison to the rest of metallofullerenes. This is especially happening for Fe and Ti metallofullerenes, which exhibit bonds closer to covalent ($1 < |V|/G < 2$). The apparently best combination for intense IR spectra is obtained for systems with a strong charge reordering, large vibrational displacement of the metal, and noticeable ionic bondings.

On the other hand, the binding of the metal to the carbon cage can generate a displacement of the pristine C_{60} features and the appearance of new lines. Two main factors seem to be responsible for the former trend: the position at which the metal is attached, and the strength of the bonds. Strong bonds are characterized by the increment of the electron density within the internuclear region, while the position determines the number of carbon bonds that is affected by the metal. Both factors can produce richer IR spectra around the four fundamental C_{60} IR features. An important point here is that the binding energy values displayed in Figures 1–4 reflect the binding strength (negative values indicate a stronger binding), but these values result from the contribution of both metal position and electron density in the internuclear region. For the former, it is very difficult to relate the binding energies per se with any possible trend observed in the simulated spectra. Table 1 displays the average internuclear electron density (ρ), the number of binding sites of the metal (B), and the position to which the metal is bonded. These parameters can be used to understand the peculiarities observed in the metallofullerene IR spectra with the metals Fe and Ti, but also other general trends. It is important to clarify that strong binding does not necessarily imply more intense IR spectra but just richer IR spectra: the IR intensity mainly depends on charge reordering and metal vibrational displacement (see above). The metals Fe and Ti are most strongly bound to the C_{60} cage by far (see ρ in Table 1), in particular, the charged metalloendofullerene with Ti, with $\rho = 24.77$ atomic units. Even though Ti is bonded to only two carbon atoms at the hexagon-asymmetric position (Hex-As), this interaction is strong enough to affect the other neighbor atoms that lie farther away and C–C bonds; the latter is translated into a much richer IR spectrum (see Figure 2). Furthermore, this richness of the spectra is also attained when the metal is at the hexagon–hexagon position (HH; see the Fe

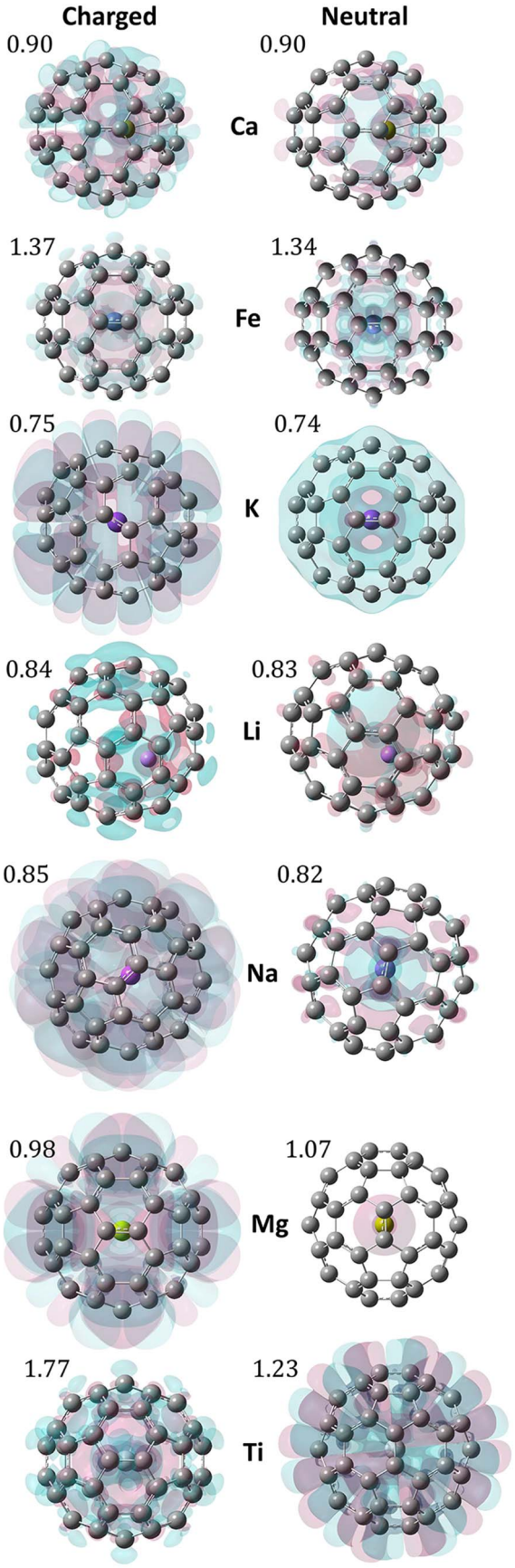

Figure 5. Charge-density difference maps of the simulated metalloendofullerenes obtained for an isovalue of 0.02 atomic units. Light red regions indicate electron depletion, while light blue regions indicate electron accumulation. In each case, the $|V|/G$ ratio is displayed in the top left corner of the model.

case in Table 1). However, the lowest ρ values displayed in Table 1 are observed for both (neutral and charged) endofullerenes with K at the cage position, exhibiting also more binding sites. This is the reason why the K endofullerenes displayed the very discrete (or weaker) IR spectra in Figures 1 and 2. The effect of the binding position of the metal seems predominant in the resulting IR spectra, especially when the metals are at similar positions; e.g., the neutral exofullerenes with Li, Na, K, and Ca display some resemblance in their spectra (see Figure 3). The general trend observed from the comparison of Table 1 with Figures 1–4 is that metals that are bonded to hexagon–hexagon (HH) sites tend to exhibit richer spectra. In fact, it is possible to establish the following decreasing order according to the metal position: HH $>$ Hex $\simeq$ Hex-As $>$ Pent $>$ PH $>$ Cage (see Table 1). Therefore, we conclude that the factors required to obtain very diverse IR spectra (i.e., in terms of spectral feature variety) are the bonding strength and the closeness of the metal to the HH position. The bonding strength, metal position, and charge reordering are thought to be intrinsically connected, but we can try to decouple their effect in order to understand and predict the IR spectra of new species.

4. Summary and Astrophysical Relevance

Quantum-chemistry calculations at the DFT/B3LYP 6-31G (d) level of theory have been performed in order to obtain the individual simulated mid-IR ($\sim$5–50 μm) spectra of 28 metallofullerene species; neutral and charged endo- and exohedral metallofullerenes for seven different metals (Li, Na, K, Ca, Mg, Ti, and Fe).

Our calculations and IR simulations show that metallofullerenes can exhibit rich or more discrete IR spectra regardless of whether they are neutral or charged. Neutral metallofullerenes have the tendency to show richer spectra in the 5–10 μm spectral region, accompanied by a considerable loss of IR intensity in the 15–20 μm range. Charged metallofullerenes, on the other hand, can display a major IR contribution in the 15–20 μm range. According to our calculations, however, there are some metallofullerene systems where the neutral species display a discrete spectrum over the full IR wavelength regime. Three key factors determine the landscape of the spectra: charge reordering, bonding strength, and metal position. The first factor is related to the intensity observed in the IR spectra, while the other two factors affect the wavelength displacement and spectral appearance of new IR features.

We conclude that richer spectral regions do not solely describe the presence of neutral species, for instance, aromatic and aliphatic carbon molecules, but also charged species with a strong binding, as is the case of some of the metallofullerenes presented here. Nevertheless, it is very important to stress that for the neutral metallofullerene species with strong charge-reordering processes, we expect a higher IR intensity in comparison to their charged counterparts.

The JWST, with a much higher sensitivity (and spectral resolution) than the previous Spitzer Space Telescope, has the required potential to unambiguously detect the spectral signatures of new IR emission features that might be due to metallofullerenes (or even other complex metal-organic species). Thus, the metallofullerene IR spectra are made publicly available to the astrophysical community, especially to users of the JWST.

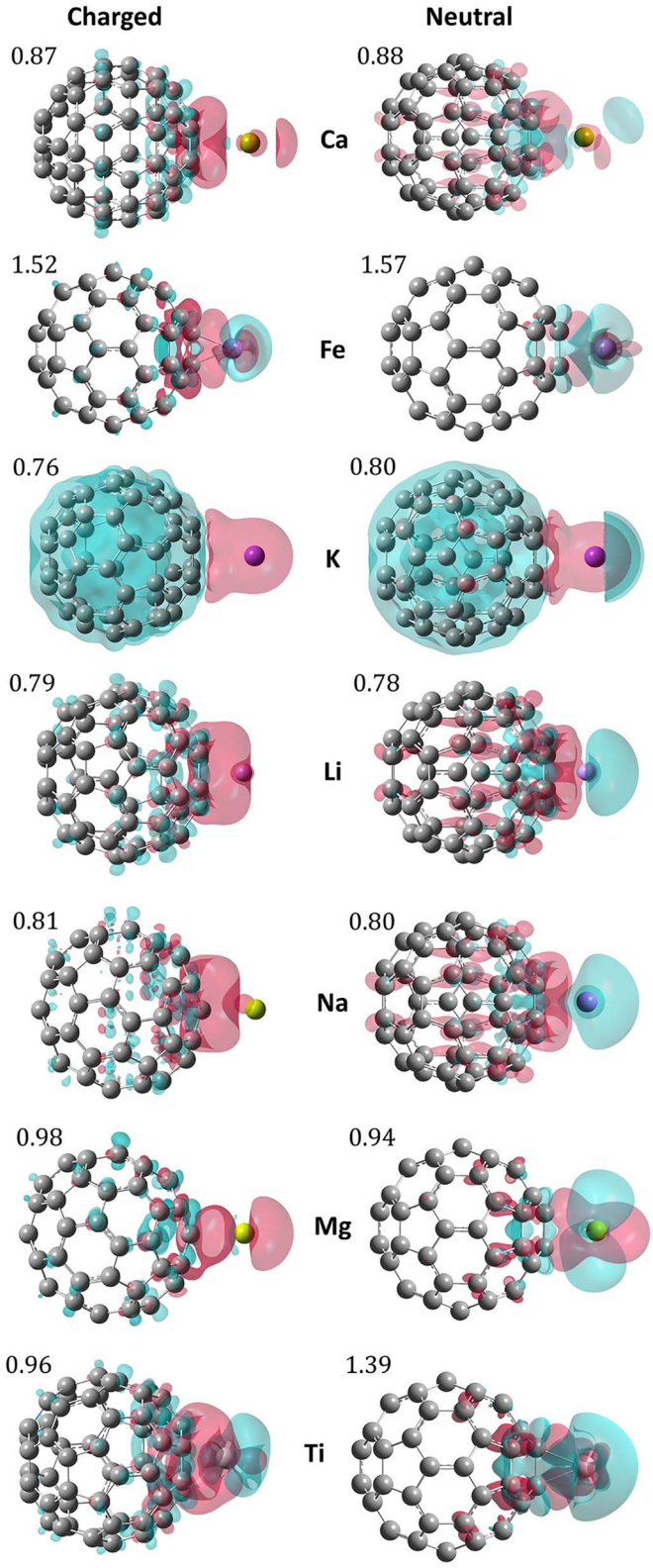

Figure 6. Charge-density difference maps of the simulated metalloexofullerenes. The notation is the same as in Figure 5.

The individual metallofullerene spectra provide several distinctive IR features of these complex metal-organic species. The metallofullerene mid-IR spectra (which can be treated as unperturbed spectra) can be used to simulate different circumstellar and interstellar environments. The goal of the current data is to permit a precise modeling of the IR emission by metallofullerene species. For this, we also provide all the individual IR line positions, accompanied by their corresponding intensities. These data can be used to build IR spectra that are representative of the metallofullerene species in several types of astronomical environments as in previous computational protocols (see, e.g., Barzaga et al. 2023), for example, depending on the thermal distribution of metallofullerenes in the circumstellar environments (Maxwell–Boltzmann distribution). Furthermore, the specific chemical abundances of the astrophysical environments, if known from observations or nucleosynthesis theoretical predictions, can be included in the simulation of the representative IR spectra of the metallofullerene species; e.g., as was previously done by Barzaga et al. (2023) and as shown in Figure 7 (see below), where the chemical abundances from nucleosynthesis models and observations where used to simulate the metallofullerene representative spectra in the circumstellar environments of PNe and RCB stars with fullerenes, respectively.

In Barzaga et al. (2023), we considered the metal abundances, possible metallofullerene formation reactions, ionization level, and endo and exo concentration to reproduce the large range of C_{60} 17.4 μm/18.9 μm band ratios observed in very different fullerene-rich circumstellar environments such as PNe and RCB stars. The simulated representative IR spectra of the metallofullerene species in two fullerene-rich objects (the PN LMC 99 and the RCB star DY Cen) are shown (for the first time) in Figure 7 in comparison with their Spitzer Space Telescope spectra. Although the Spitzer IR spectra have a lower spectral resolution and sensitivity than those of the JWST, Figure 7 shows that metallofullerenes contribute significantly to the IR bands of neutral C_{60} in circumstellar environments showing very different C_{60} 17.4 μm/18.9 μm band ratios. The representative metallofullerene simulated IR spectra are consistent with the Spitzer observations, even assuming that metallofullerenes are the only emitters causing the 17.4 μm/18.9 μm anomaly in the spectra. From this exercise, we conclude that the metallofullerene species expected to be present in space would depend on the specific physicochemical properties of the circumstellar environment (i.e., metal abundances, formation reactions, ionization level, and endo and exo concentration), but the more prevalent metallofullerene species are generally those with the most abundant metals, such as Mg and Fe (see also Barzaga et al. 2023).

We remark that the individual spectra of all the metallofullerene species considered here display IR emission close to the four strongest IR features of neutral C_{60} as well as a series of discrete features in the 6–9 μm spectral region, which can be of similar strength (exo species) or stronger (endo species) than the pristine C_{60} features (see Figures 1–4). The rest of IR features are more specific to each metallofullerene species and are generally weaker. A detailed comparison of the 28 individual metallofullerene mid-IR simulated spectra with the available Spitzer spectral data of fullerene-rich sources is beyond the scope of this paper. For example, PNe with fullerenes display the general presence of a broad and complex (with multiple components/peaks and blends) IR feature at ~6–9 μm (e.g., Bernard-Salas et al. 2012; García-Hernández et al. 2012; Sloan et al. 2014) that would be consistent (after intensity scaling) with most of the individual metallofullerene simulated spectra (e.g., Hou et al. 2023), but not enough so to

Table 1
Properties of the Metal–C_{60} Bonding in Metallofullerenes

	Endofullerenes						Exofullerenes					
	Neutral			Charged			Neutral			Charged		
	ρ	B	Position	ρ	B	Position	ρ	B	Position	ρ	B	Position
Ca	2.27	2	HH	2.18	2	HH	1.70	2	Hex-As	1.27	5	Pent
Mg	0.72	37	Cage	1.92	1	HH	2.96	2	HH	2.45	1	PH
Li	2.15	1	Hex	2.06	3	Hex	1.79	1	Hex-As	1.30	3	Hex
Na	1.17	1	HH	1.09	2	PH	1.40	2	Hex-As	1.01	3	Hex
K	0.39	34	Cage	0.40	60	Cage	1.16	2	Hex	0.78	3	Hex
Fe	8.46	2	HH	8.49	2	HH	8.86	2	HH	9.97	2	HH
Ti	8.84	2	Hex-As	24.77	2	HH	9.47	2	HH	3.94	6	Hex

Note. ρ: average of the electron density within the internuclear region in atomic units. B: number of sites to which the metal is bonded. Position: the position of the metal in the carbon cage. HH: the metal is connected in a hexagon–hexagon bond region. Hex: center of a hexagon. Hex-As: slightly offset from the hexagon center. PH: pentagon–hexagon bond. Pent: center of a pentagon. Cage: center of C_{60}.

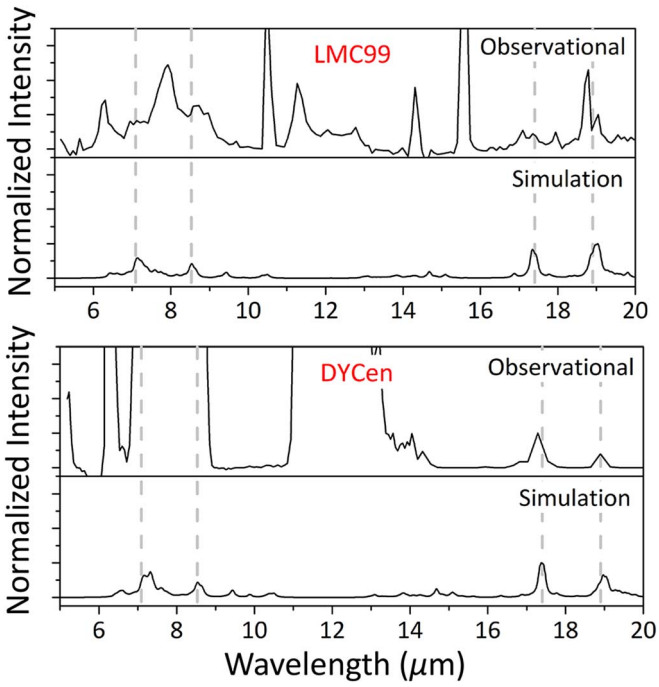

Figure 7. Comparison of the continuum-subtracted Spitzer Space Telescope (top) and representative metallofullerene simulated IR spectra (bottom) for two fullerene-rich objects showing very different C_{60} 17.4 μm/18.9 μm band ratios and chemical abundances: the PN LMC 99, and the RCB star DY Cen. The guidelines show the features of pristine C_{60} at 7.09, 8.53, 17.34, and 18.91 μm, according to our calculations. The representative metallofullerene simulated spectra correspond to the simulations by Barzaga et al. (2023), which consider the metal abundances, ionization level, and endo and exo concentration (see Barzaga et al. 2023, for more details), and reproduce the observed 17.4 μm/18.9 μm band ratios. The intensity has been normalized according to the 17.4 μm/18.9 μm band ratio under the assumption that metallofullerenes are the only emitters causing the 17.4 μm/18.9 μm anomaly in the spectra; i.e., the more intense feature of the 17.4 μm/18.9 μm pair has been used to establish the reference in the normalization.

claim their detection/identification. In addition, comparisons like this would not consider the metal abundances, possible metallofullerene formation reactions, ionization level, and endo and exo concentration in the circumstellar environments around PNe (see above). In short, the quantum-chemistry-simulated metallofullerene IR spectra presented here can be combined with astrophysical models, and their comparison with real JWST data could eventually lead to the detection of these complex metal-organic species in space.

Acknowledgments

We acknowledge support from the ACIISI, Gobierno de Canarias, and the European Regional Development Fund (ERDF) under a grant with reference PROID2020010051 as well as the State Research Agency (AEI) of the Spanish Ministry of Science and Innovation (MICINN) under grants PID2020-115758GB-I00 and PID2019-110091GB-I00 and the "María de Maeztu" (CEX2018-000805-M) Program for Centers of Excellence in R&D. This article is based upon work from COST Action NanoSpace, CA21126, supported by the European Cooperation in Science and Technology (COST). We acknowledge the generous allocation of computer time at the Centro de Computación Científica at the Universidad Autónoma de Madrid (CCC-UAM) and at the La Palma Supercomputer at the Instituto de Astrofísica de Canarias.

ORCID iDs

R. Barzaga https://orcid.org/0000-0002-9827-2762
D. A. García-Hernández https://orcid.org/0000-0002-1693-2721
S. Díaz-Tendero https://orcid.org/0000-0001-6253-6343
SeyedAbdolreza Sadjadi https://orcid.org/0000-0003-3529-0178
A. Manchado https://orcid.org/0000-0002-3011-686X
M. Alcami https://orcid.org/0000-0002-3753-5215
M. A. Gómez-Muñoz https://orcid.org/0000-0002-3938-4211
T. Huertas-Roldán https://orcid.org/0000-0002-5523-2568

References

Bader, R. 1990, Atoms in Molecules: A Quantum Theory (Oxford: Oxford Univ. Press)
Barzaga, R., García-Hernández, D., Díaz-Tendero, S., et al. 2023, ApJ, 942, 5
Barzaga, R., Lestón-Sánchez, L., Aguilar-Galindo, F., Estévez-Hernández, O., & Díaz-Tendero, S. 2021, InCh, 60, 11984
Becke, A. D. 1993, JChPh, 98, 5648
Bernard-Salas, J., Cami, J., Peeters, E., et al. 2012, ApJ, 757, 41
Cami, J., Bernard-Salas, J., Peeters, E., & Malek, S. E. 2010, Sci, 329, 1180
Cernicharo, J., Cabezas, C., Pardo, J. R., et al. 2023, A&A, 672, L13
Cernicharo, J., & Guelin, M. 1987, A&A, 183, L10
Cremer, D., & Kraka, E. 1984, Croatica Chemica Acta, 57, 1259, https://hrcak.srce.hr/194019

Ditchfield, R., Hehre, W. J., & Pople, J. A. 1971, JChPh, 54, 724
Dunk, P. W., Adjizian, J. J., Kaiser, N. K., et al. 2013, PNAS, 110, 18081
Frisch, M. J., Trucks, G. W., Schlegel, H. B., et al. 2016, Gaussian 16 Revision C.01 (Wallingford, CT: Gaussian, Inc.)
García-Hernández, D. A., Kameswara Rao, N., & Lambert, D. L. 2011, ApJ, 729, 126
García-Hernández, D. A., Manchado, A., García-Lario, P., et al. 2010, ApJL, 724, L39
García-Hernández, D. A., Villaver, E., García-Lario, P., et al. 2012, ApJ, 760, 107
Highberger, J., Savage, C., Bieging, J., & Ziurys, L. 2001, ApJ, 562, 790
Hou, G.-L., Lushchikova, O. V., Bakker, J. M., et al. 2023, ApJ, 952, 13
Jeffery, C. S., Karakas, A. I., & Saio, H. 2011, MNRAS, 414, 3599
Jones, D., & Boffin, H. M. 2017, NatAs, 1, 0117
Karakas, A. I., & Lattanzio, J. C. 2014, PASA, 31, e030
Keith, T. A., 2019 AIMAll, v19.10.12 (Overland Park KS: TK Gristmill Software), http://aim.tkgristmill.com/
Kern, B., Strelnikov, D., Weis, P., Böttcher, A., & Kappes, M. M. 2013, JPCA, 117, 8251
Kwitter, K. B., & Henry, R. 2022, PASP, 134, 022001
McGuire, B. A. 2022, ApJS, 259, 30
Montiel, E. J., Clayton, G. C., Sugerman, B., et al. 2018, AJ, 156, 148
Pandey, G., Hema, B., & Reddy, A. B. 2021, ApJ, 921, 52
Pech, C., Joblin, C., & Boissel, P. 2002, A&A, 388, 639
Pradhan, A. K., & Nahar, S. N. 2011, Atomic Astrophysics and Spectroscopy (Cambridge: Cambridge Univ. Press)
Robledo, M., Aguirre, N. F., Díaz-Tendero, S., Martín, F., & Alcamí, M. 2014, RSCAd, 4, 53010
Schwab, J. 2019, ApJ, 885, 27
Sloan, G. C., Lagadec, E., Zijlstra, A. A., et al. 2014, ApJ, 791, 28
Snow, T. P., Zukowski, D., & Massey, P. 2002, ApJ, 578, 877
Zabardasti, A., Afrouzi, H., Kakanejadifard, A., & Jamshidi, Z. 2017, J. Sulfur Chem., 38, 249
Zapata Trujillo, J. C., & McKemmish, L. K. 2022, WIREs Comput. Mol. Sci., 12, e1584
Ziurys, L. M. 2006, PNAS, 103, 12274